J Mater Sci: Mater Med (2012) 23:2867–2879
DOI 10.1007/s10856-012-4767-3

Magnesium- and strontium-co-substituted hydroxyapatite: the effects of doped-ions on the structure and chemico-physical properties

Valentina Aina · Gigliola Lusvardi · Basil Annaz · Iain R. Gibson · Flora E. Imrie · Gianluca Malavasi · Ledi Menabue · Giuseppina Cerrato · Gianmario Martra

Received: 11 July 2012 / Accepted: 15 September 2012 / Published online: 29 September 2012

Abstract The present study is aimed at investigating the contribution of two biologically important cations, Mg^{2+} and Sr^{2+}, when substituted into the structure of hydroxyapatite ($Ca_{10}(PO_4)_6(OH)_2$,HA). The substituted samples were synthesized by an aqueous precipitation method that involved the addition of Mg^{2+}- and Sr^{2+}-containing precursors to partially replace Ca^{2+} ions in the apatite structure. Eight substituted HA samples with different concentrations of single (only Mg^{2+}) or combined (Mg^{2+} and Sr^{2+}) substitution of cations have been investigated and the results compared with those of pure HA. The obtained materials were characterized by X-ray powder diffraction, specific surface area and porosity measurements (N_2 adsorption at 77 K), FT-IR and Raman spectroscopies and scanning electron microscopy. The results indicate that the co-substitution gives rise to the formation of HA and β-TCP structure types, with a variation of their cell parameters and of the crystallinity degree of HA with varying levels of substitution. An evaluation of the amount of substituents allows us to design and prepare BCP composite materials with a desired HA/β-TCP ratio.

V. Aina · G. Cerrato · G. Martra
Department of Chemistry, University of Turin, Via P. Giuria 7, 10125 Turin, Italy

V. Aina · G. Cerrato · G. Martra
Centre of Excellence NIS (Nanostructured Interfaces and Surfaces), INSTM (Italian National Consortium for Materials Science and Technology), UdR University of Torino, Turin, Italy

G. Lusvardi (✉) · G. Malavasi · L. Menabue
Department of Chemistry, University of Modena and Reggio Emilia, Via Campi 183, 41125 Modena, Italy
e-mail: gigliola.lusvardi@unimore.it

B. Annaz · I. R. Gibson · F. E. Imrie
School of Medical Sciences, Institute of Medical Sciences, University of Aberdeen, Foresterhill, Aberdeen AB25 2ZD, UK

1 Introduction

Hydroxyapatite ($Ca_{10}(PO_4)_6(OH)_2$,HA) [1] is widely used in production of osteoconductive ceramic materials for orthopedic and dental applications [2–8]. In order to improve some features of the apatitic bone substitutes, such as osteointegration, mechanical properties and implantation efficacy, HA ceramics can be doped with small amounts of ions that are found in natural bone mineral [9–13].

Many studies have focused on the effect of single ionic substitutions in the HA structure which have proven to be easier in terms of synthesis and structural characterization [9, 14–16]. From a materials science viewpoint, the structural characterization of ionic substituted HA is essential, given the trace levels of ionic substitutions found both in natural bone and tooth mineral. There are a general lack of studies that investigate coupled ionic substitutions in the HA structure. Co-substituting two different ions, by balancing contrasting ionic radii and/or valence, offers the possibility of substituting ions that are difficult to substitute alone, such as magnesium ions [17], or of substituting a greater level of an ionic substituent, such as silicate ions [18].

The present study is an attempt to develop a coupled ionic substitution HA involving two important trace elements, namely magnesium (Mg^{2+}) and strontium (Sr^{2+}).

Magnesium is a fundamental element and prevents possible risk factors for osteoporosis in humans [1]. Magnesium also has its own significance in the calcification process, bone fragility and an indirect influence on mineral metabolism [16, 19, 20].

Strontium is considered as a bone-seeking element that presents a beneficial effect on bone growth [21]. Its ability to decrease bone resorption and to enhance bone formation in vivo has also been proved [22, 23].

Although several articles have already been published on the chemico-physical properties of apatites and substituted apatites, only a few works were devoted to careful investigation of Mg^{2+}-doped HA [10, 14, 24–26] and no paper reports the study of co-substitution of Sr^{2+} and Mg^{2+} in HA. The paper of *Kannan* et al. [19]. recently reported the synthesis and structural characterization of Sr^{2+}- and Mg^{2+}-co-substituted β-tricalcium phosphate (β-$Ca_3(PO_4)_2$, β-TCP). Considering the importance of Sr and Mg as essential elements, we report here the synthesis and characterization of Sr^{2+}- and Mg^{2+}-co-substitution in HA.

The synthesis of substituted hydroxyapatites can be performed either by a solid state route or by an aqueous precipitation method; in this paper, an aqueous precipitation route to form both Mg-substituted HA and Sr^{2+}- and Mg^{2+}-co-substituted HA is reported. This method is based on the addition of Mg^{2+} and Sr^{2+} containing precursors to partially replace Ca^{2+} in the HA composition. Eight HA derived samples with different concentrations of single or combined substituting elements were prepared in the present investigation and structural information on the influence of these ions on co-substituted HA was gained using different experimental techniques.

2 Materials and methods

2.1 Synthesis

Non-substituted and substituted hydroxyapatites were prepared by aqueous precipitation.

To synthesize 0.01 mol of hydroxyapatite, 0.10 mol of calcium hydroxide ($Ca(OH)_2$, Sigma) and 0.06 mol of phosphoric acid (H_3PO_4, Sigma) were combined in a 10:6 molar ratio. Calcium hydroxide was stirred magnetically in 200 mL of distilled water for 20 min until a homogeneous suspension was obtained. Phosphoric acid (diluted with 200 mL of distilled water) was added dropwise to this solution over 45 min, with continuous stirring, with the pH maintained above 10.5 by addition of ammonia solution, as necessary. The solution was stirred for a further 2 h, and then allowed to stand overnight, after which the product was filtered under suction and dried in ambient conditions. All the reaction steps were carried out at room temperature (RT).

Magnesium-substituted hydroxyapatites were prepared by an analogous method, but with a reduction of the amount of Ca^{2+} and an addition of an equimolar amount of Mg^{2+} in the form of magnesium chloride hexahydrate ($MgCl_2{\cdot}6H_2O$, Sigma).

Similarly for Sr^{2+}- and Mg^{2+}-co-substituted hydroxyapatites, the amount of Ca^{2+} was reduced with addition of an equimolar amount of bivalent cations in the form of strontium nitrate ($Sr(NO_3)_2$, Sigma) and $MgCl_2{\cdot}6H_2O$. Landi et al. reported the effectiveness of $MgCl_2$ as a reactant in the synthesis by aqueous precipitation of biomimetic Mg-substituted hydroxyapatite, and did not indicate any unwanted co-substitution of the product MgHA structure by chloride ions. These results supported our choice of $MgCl_2$ over $MgNO_3$ as the Mg^{2+} source in our synthesis method. [27].

As in the preparation of pure hydroxyapatite, the pH was continuously monitored throughout the synthesis.

For all compositions the design composition was a (Ca + X)/P molar ratio of 1.667, where X = Mg + Sr.

Desired compositions of the synthesized samples and molar concentrations of reactants used are given in Table 1.

The powders were heated in a high temperature furnace (Carbolite). Samples were heated from 200 to 1,100 °C at 10 °C/min, holding at 1,100 °C for 16 h, followed by cooling the products from 1,100 to 200 °C at 10 °C/min and then air-cooling to RT.

Table 1 Molar concentrations of reactants and metal/phosphorus molar ratios

Desired composition	Molar concentration of reactants				(Ca + X)/P molar ratio (X = Mg and/or Sr)
	$Ca(OH)_2$	H_3PO_4	$Sr(NO_3)_2$	$MgCl_2{\cdot}6H_2O$	
$Ca_{10}(PO_4)_6(OH)_2$	0.100	0.06	–	–	1.67
$Ca_{9.9}Mg_{0.1}(PO_4)_6(OH)_2$	0.099	0.06	–	0.001	1.67
$Ca_{9.5}Mg_{0.5}(PO_4)_6(OH)_2$	0.095	0.06	–	0.005	1.67
$Ca_9Mg_1(PO_4)_6(OH)_2$	0.090	0.06	–	0.010	1.67
$Ca_9Mg_{0.1}Sr_{0.9}(PO_4)_6(OH)_2$	0.090	0.06	0.009	0.001	1.67
$Ca_9Mg_{0.5}Sr_{0.5}(PO_4)_6(OH)_2$	0.090	0.06	0.005	0.005	1.67
$Ca_8Mg_{0.1}Sr_{1.9}(PO_4)_6(OH)_2$	0.080	0.06	0.019	0.001	1.67
$Ca_8Mg_{0.5}Sr_{1.5}(PO_4)_6(OH)_2$	0.080	0.06	0.015	0.005	1.67
$Ca_8Mg_1Sr_1(PO_4)_6(OH)_2$	0.080	0.06	0.010	0.010	1.67

2.2 Methods

All analysis was performed on samples (in the powder form) heated at 1,100 °C, unless otherwise stated.

2.2.1 X-ray powder diffraction (XRPD)

XRPD analysis was performed on powder samples using a Bragg–Brentano diffractometer (PANalytical X'Pert Pro, Ni-filtered Cu Kα source), a 3–110° 2θ range and a counting time of 50 s for each 0.03° (2θ step). Diffraction patterns were compared to ICDD database PDF patterns [28] of $Ca_{10}(PO_4)_6(OH)_2$ (HA, JCPDS no. 09-432) and β-$Ca_3(PO_4)_2$ (β-TCP, JCPDS no. 09-0169).

The degree of crystallinity of the HA phase, corresponding to the fraction of crystalline phase (X_c) in the HA powders, was evaluated by the following equation (1) [29].

$$X_c \approx 1 - \frac{V_{112/300}}{I_{300}} \quad (1)$$

where I_{300} is the intensity of (300) *hkl* reflection and $V_{112/300}$ is the background intensity of the space between (112) *hkl* and (300) *hkl* reflections.

Rietveld refinements were performed with GSAS [30] and EXPGUI programs [31]. Initial atomic coordinates and unit cell dimensions were taken from previously published data; the structural models are from the ICSD database: card numbers 26205 for HA and 6191 for β-$Ca_3(PO_4)_2$ [32, 33]. Parameters varied in the refinement were atomic coordinates (x, y and z), unit cell parameters (*a* and *c*), displacement parameters (Uiso), peak intensity scaling and peak profile parameters related to particle size.

2.2.2 Scanning electron microscopy—energy dispersive spectroscopy (SEM/EDS)

The composition of synthesized materials was determined by means of SEM (FEI Quanta 200, FEI Company), equipped with an EDS instrument (INCA 350, Oxford Instruments). For each composition, three different samples were analyzed, and the EDS analysis was performed over 20 different sample areas ($\sigma = 0.5$ %). Results were validated by comparison with reference standards.

2.2.3 Specific surface area (SSA) and porosity measurements

Specific surface area of unheated powders was evaluated using a micromeritics ASAP 2020 porosimeter, by adsorption of an inert gas (N_2) at 77 K. Before measurements, all samples were activated *in vacuo* (residual pressure $<10^{-3}$ Torr) at room temperature for 12 h in order to remove physisorbed atmospheric contaminants. For SSA determination, data were analyzed with the BET model. The accuracy of the conventional BET method/model for SSA determination is known to be relatively low (±5 % divergence from the actual area), even if the instrumental accuracy and reproducibility of data obtained with modern automatic gas-volumetric instrumentation is quite high (±0.2 %). The BJH (Barrett-Joyner-Halenda) model was used to analyze mesopores, and the "t-plot" (statistical thickness) method was employed to evaluate the presence of micropores [34].

2.2.4 Raman spectroscopy

Raman spectra were recorded using a Renishaw inVia Raman microscope spectrometer. A diode laser emitting at 785 nm was used, which had an output power of 65 mW at the sample. Photons scattered by the sample were dispersed by a 1,200 lines/mm grating monochromator, and simultaneously collected on a CCD camera; the collection optic was set at 20 d ULWD objective (5 μm diameter laser spot). The spectra collection setup of ten acquisitions, each taking 10 s, was adopted.

2.2.5 Attenuated total reflectance (ATR) spectroscopy

IR spectra were recorded on a Nicolet 5700 FTIR spectrometer, equipped with a smart orbit diamond ATR accessory and a DTGS detector; the spectral resolution was 4 cm^{-1} and the number of scans for each spectrum was 128.

3 Results and discussion

3.1 X-ray powder diffraction

The results derived from the collected diffraction patterns and from Rietveld refinements of these data are reported in Table 2; diffraction patterns of all samples are reported in Fig. 1 and in particular, some representative patterns showing more detail are reported in Fig. 2.

In the case of the $Ca_{10}(PO_4)_6(OH)_2$ and $Ca_{9.9}Mg_{0.1}(PO_4)_6(OH)_2$ samples, peak positions and relative intensities correspond very well to those of the ICDD PDF pattern for stoichiometric HA. A slight reduction of peak intensity counts for Mg^{2+}-containing apatite is in agreement with a similar behaviour of the crystallinity (96 and 94 % for $Ca_{10}(PO_4)_6(OH)_2$ and $Ca_{9.9}Mg_{0.1}(PO_4)_6(OH)_2$, respectively); however, the small molar amount (0.1 mol) of Mg^{2+} does not influence significantly the cell parameter values. At increasing amounts of Mg^{2+} (0.5 and 1 mol), in addition to the peaks of an HA phase, other peaks were identified that were characteristic of a β-TCP phase.

Table 2 Data obtained by XRPD analysis

Samples	Phases[a]	Intensity(counts)	d (Å) (I_{121})	Position (°2θ) (I_{121})	Crystallinity degree of HA *Xc* (% ± 4)	HA/ β-TCP ratio	$a = b$ (Å)[b]	c (Å)[b]
$Ca_{10}(PO_4)_6(OH)_2$	HA	7,806	2.82	31.77	96	–	9.422(3)	6.880(5)
$Ca_{9.9}Mg_{0.1}(PO_4)_6(OH)_2$	HA	6,555	2.82	31.77	94	–	9.421(2)	6.878(5)
$Ca_{9.5}Mg_{0.5}(PO_4)_6(OH)_2$	HA	5,181	2.83	31.63	93	0.74/0.26	9.437(3)	6.870(4)
	β-TCP	1,827	2.87	31.14			10.346(1)	37.162(3)
$Ca_9Mg_1(PO_4)_6(OH)_2$	HA	2,991	2.80	31.98	89	0.48/0.52	9.423(2)	6.877(3)
	β-TCP	3,279	2.84	31.52			10.360(2)	37.174(5)
$Ca_9Mg_{0.1}Sr_{0.9}(PO_4)_6(OH)_2$	HA	7,356	2.84	31.53	91	0.81/0.19	9.501(4)	6.840(5)
	β-TCP	1,682	2.86	30.85			10.377(3)	37.167(3)
$Ca_9Mg_{0.5}Sr_{0.5}(PO_4)_6(OH)_2$	HA	4,785	2.85	31.37	80	0.94/0.06	9.463(5)	6.911(5)
	β-TCP	281	2.88	31.01			10.440(1)	37.635(6)
$Ca_8Mg_{0.1}Sr_{1.9}(PO_4)_6(OH)_2$	HA	4,166	2.84	31.44	80	0.74/0.26	9.493(4)	6.924(4)
	β-TCP	1,427	2.92	30.63			10.495(2)	37.846(5)
$Ca_8Mg_{0.5}Sr_{1.5}(PO_4)_6(OH)_2$	HA	2,958	2.85	31.35	73	0.54/0.46	9.489(2)	6.905(2)
	β-TCP	2,495	2.89	30.94			10.463(1)	37.332(3)
$Ca_8Mg_1Sr_1(PO_4)_6(OH)_2$	HA	2,732	2.85	31.44	68	0.46/0.54	9.510(3)	6.889(4)
	β-TCP	3,176	2.88	31.03			10.409(2)	37.385(3)

[a] The structure model of these phases has been used for the Rietveld refinement

[b] Theoretical values for HA and β-TCP are, respectively: $a = b = 9.424(4)$ (Å), $c = 6.879(4)$ (Å) and $a = b = 10.429(2)$ (Å), $c = 37.380(3)$ (Å)

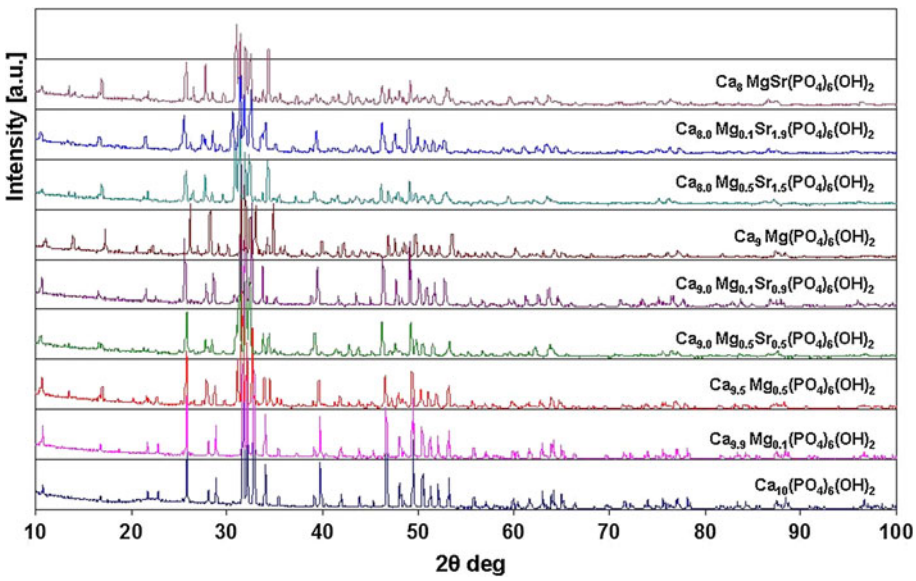

Fig. 1 XRD patterns of all samples

Counts of the peak intensities related to the β-TCP structure type increased with the content of Mg^{2+} and at the same time the quantity of the HA phase diminished, as confirmed from the changing ratio between the phases HA and β-TCP; the HA/β-TCP ratio varied from ~3 (approximately 75/25 %) to ~1 (approximately 50/50 %), respectively for 0.5 and 1 mol of Mg^{2+}.

A reduction in the crystallinity degree of the HA phase was also observed at the highest amount of Mg^{2+}: 89 % for $Ca_9Mg_1(PO_4)_6(OH)_2$ compared to 96 % for pure $Ca_{10}(PO_4)_6(OH)_2$.

The smaller dimension of Mg^{2+} (72 pm) compared to Ca^{2+} (100 pm) also influences the cell parameters in terms of a contraction of their values; this was especially evident in the β-TCP phase, with a reduction of both *a* and *c* axes. These results are in agreement with the well-documented behaviour of Mg^{2+} towards apatites [35]; the presence of Mg^{2+} strongly influences the crystallinity, morphology,

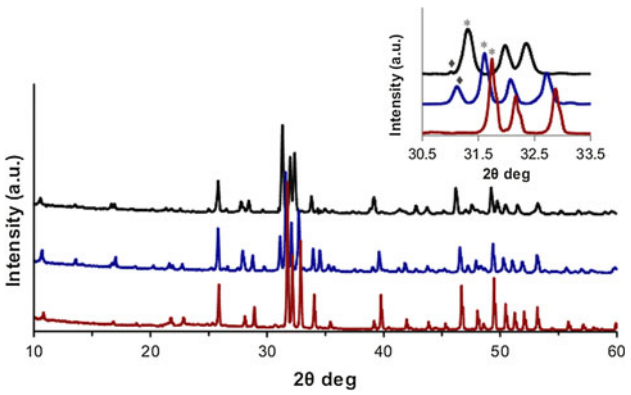

Fig. 2 XRD patterns of $Ca_{10}(PO_4)_6(OH)_2$ (*brown line*); $Ca_{9.5}Mg_{0.5}(PO_4)_6(OH)_2$ (*blue line*); $Ca_9Mg_{0.5}Sr_{0.5}(PO_4)_6(OH)_2$ (*black line*). Intensity is reported in arbitrary units. Patterns have been y-axis shifted for display purposes. *Inset*: Details in the 30.5–33.5° 2θ range and I_{100} peaks of HAP (*asterisk*) and β-TCP (*black diamond*) (Color figure online)

crystal size and thermal stability of HA and also favours the formation and stabilization of β-TCP. However, in the present study the unit cell dimensions of the HA phase do not show a significant reduction with increasing Mg substitution, as observed in other studies of non-heated Mg-substituted apatites [18, 36].

In relation to Sr^{2+}- and Mg^{2+}-co-substitution, in all cases it is possible to recognize characteristic peaks of HA and β-TCP phases; the combined effect of Mg^{2+} and Sr^{2+} ions influences the crystallinity degree of HA, the HA/β-TCP ratio, and the cell parameters. In particular, if we compare the results at a fixed Ca^{2+} amount, starting with the $Ca_9Mg_{0.1}Sr_{0.9}(PO_4)_6(OH)_2$ and $Ca_9Mg_{0.5}Sr_{0.5}(PO_4)_6(OH)_2$ samples, the higher amount of Mg^{2+} and correspondingly the lower amount of Sr^{2+} decreases the crystallinity degree of the HA phase (from 91 to 80 %, respectively) and increases the HA/β-TCP ratio (from approximately 81–94 %, respectively).

In the first sample ($Ca_9Mg_{0.1}Sr_{0.9}(PO_4)_6(OH)_2$), looking at the cell parameter values, it is assumed that the higher amount of Sr^{2+} influences the HA structure in particular, with an expansion of cell parameters, especially evident for the *a* axis, from 9.501 Å compared to 9.424 Å for pure HA; this is consistent with the slightly larger ionic radius of Sr^{2+} compared to Ca^{2+} (118 and 100 pm, respectively). Moreover, Mg^{2+} may be more associated with the β-TCP phase, as indicated by a decrease of its cell parameters: *a* and *c* axes being 10.377 Å and 37.167 Å, respectively, compared to 10.42 and 37.380 Å for pure β-TCP. In the second sample ($Ca_9Mg_{0.5}Sr_{0.5}(PO_4)_6(OH)_2$), a higher amount of Mg^{2+} also influences the HA structure in terms of contraction of cell parameters compared to the previous values (especially evident for the *a* axis, 9.463 Å compared to the previous 9.501 Å) and, opposite to the behaviour of Sr^{2+}, reduces the crystallinity degree of HA (80 %); however, the effect of Sr^{2+} again cannot be neglected, with both HA and β-TCP phases showing increased values of the cell parameters.

For $Ca_8Mg_{0.1}Sr_{1.9}(PO_4)_6(OH)_2$, $Ca_8Mg_{0.5}Sr_{1.5}(PO_4)_6(OH)_2$ and $Ca_8Mg_1Sr_1(PO_4)_6(OH)_2$, a higher Sr^{2+} amount influences both HA and β-TCP structures with an expansion of cell parameters. Specifically, this is evident when looking at the *a* axes of both phases, namely 9.493 Å compared to 9.424 Å for pure HA and 10.495 Å compared to 10.429 Å for pure β-TCP. In the case of equimolar amounts of Sr^{2+} and Mg^{2+} and consequently Mg^{2+} at its highest value, the β-TCP structure is especially influenced, with a greater contraction of the cell parameters with respect to the previous values ($a = 10.409$ Å). An increase of Mg^{2+} also gives rise to a reduction in the degree of crystallinity of HA (80, 73 and 68 % respectively for the above mentioned samples) and a decrease of the HA/β-TCP ratio.

The co-substitution of Sr^{2+} did have a stabilising effect for the Mg^{2+} substitution level of 0.5 mol; without Sr^{2+} substitution, the composition $Ca_{9.5}Mg_{0.5}(PO_4)_6(OH)_2$ contained approximately 26 % β-TCP whereas $Ca_9Mg_{0.5}Sr_{0.5}(PO_4)_6(OH)_2$ composition contained only ~6 % β-TCP (XRD patterns shown in Figs. 1, 2). For these two compositions, which have the same level of Mg^{2+} substitution, the unit cell parameters of both phases showed an increase when Sr^{2+} was co-substituted. These co-substitution levels may correspond to values that are close to optimum for enabling appreciable Mg^{2+} substitution in the HA phase without the formation of β-TCP as a second phase. For the other two cases where the level of Mg^{2+} substitution can be considered as being constant (either 0.1 or 1 mol), and considering the phase compositions with or without Sr^{2+} co-substitution, there is either a destabilising effect of co-substitution (in the case of 0.1 mol Mg^{2+} substitution) or little effect (in the case of 1 mol Mg^{2+} substitution); for all these cases the degree of crystallinity of the HA phase decreases with Sr^{2+}co-substitution.

These results indicate that Mg^{2+} and Sr^{2+}, when simultaneously present, interact with both HA and β-TCP phases in terms of variation of cell parameters and the degree of crystallinity of the HA phase; the previous careful evaluation of the different molar ratios of the cations would allow biphasic materials with selected ratios of HA and β-TCP and also with controlled crystallinity degrees of HA to be obtained.

3.2 ESEM/EDS

In Fig. 3, areas of the investigated samples are shown. In all cases the morphology is quite irregular in term of dimensions (5–40 μm) and shape (generally, rectangular and very sharp). The samples with a lower degree of crystallinity of HA showed more irregularities in the shape

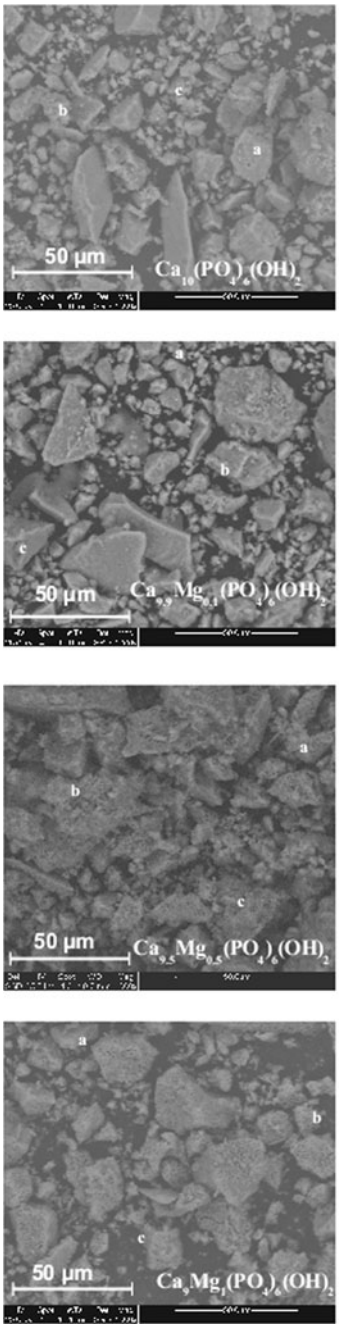

Fig. 3 SEM micrographs of the investigated samples and corresponding molar ratios derived from EDS analysis

		Ca/P experimental/theoretical	Mg/P experimental/theoretical
$Ca_{10}(PO_4)_6(OH)_2$			
	a	1.68/1.67	/
	b	1.66/1.67	/
	c	1.70/1.67	/
$Ca_{9.9}Mg_{0.1}(PO_4)_6(OH)_2$			
	a	1.66/1.65	0.02/0.02
	b	1.41/1.65	0.03/0.02
	c	1.84/1.65	0.01/0.02
$Ca_{9.5}Mg_{0.5}(PO_4)_6(OH)_2$			
	a	1.62/1.58	0.09/0.08
	b	1.35/1.58	0.11/0.08
	c	1.77/1.58	0.04/0.08
$Ca_9Mg_1(PO_4)_6(OH)_2$			
	a	1.49/1.50	0.15/0.17
	b	1.26/1.50	0.18/0.17
	c	1.60/1.50	0.07/0.17

and outlines of the aggregates. The compositions determined by semi-quantitative EDS analysis, performed by an accurate evaluation of different areas, indicate a non-homogeneous distribution of the elements that is consistent with the presence of two phases with HA and β-TCP structure and substituted with Mg^{2+} or with Mg^{2+} and Sr^{2+} simultaneously. However, it is possible to identify, always from a semi-quantitative approach, some areas with molar ratios similar to those of the nominal compositions given in Table 1. The experimental EDS molar ratios showed a good correspondence to their theoretical values in some cases. The formation of solid solutions with the nominal compositions of Table 1 cannot be excluded; unfortunately the simultaneous presence of several phases inhibits a correct and unambiguous identification of them. There was no evidence of the presence of chlorine in the analyzed samples.

3.3 SSA and porosity data

SSA and porosity data for all synthesized samples (prior to heating at 1,100 °C) are reported in Table 3. The SSAs of all materials are in the range between 70–125 m^2/g. The synthesis by an aqueous precipitation method gives rise to

Fig. 3 continued

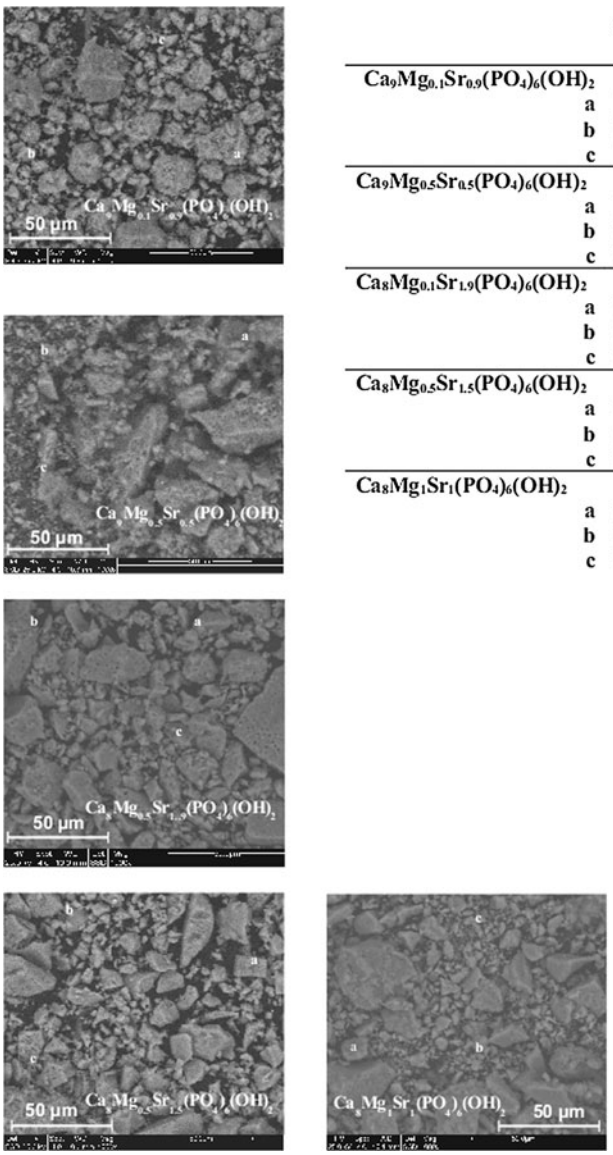

	Ca/P	Mg/P	Sr/P
	experimental/theoretical		
$Ca_9Mg_{0.1}Sr_{0.9}(PO_4)_6(OH)_2$			
a	1.49/1.50	0.02/0.02	0.14/0.15
b	1.25/1.50	0.02/0.02	0.17/0.15
c	1.56/1.50	0.03/0.02	0.02/0.15
$Ca_9Mg_{0.5}Sr_{0.5}(PO_4)_6(OH)_2$			
a	1.48/1.50	0.04/0.08	0.06/0.08
b	1.32/1.50	0.21/0.08	0.13/0.08
c	1.78/1.50	0.06/0.08	0.16/0.08
$Ca_8Mg_{0.1}Sr_{1.9}(PO_4)_6(OH)_2$			
a	1.29/1.33	0.01/0.02	0.27/0.32
b	1.21/1.33	0.02/0.02	0.24/0.32
c	1.60/1.33	0.01/0.02	0.30/0.32
$Ca_8Mg_{0.5}Sr_{1.5}(PO_4)_6(OH)_2$			
a	1.31/1.33	0.09/0.08	0.22/0.25
b	1.50/1.33	0.07/0.08	0.21/0.25
c	1.05/1.33	0.05/0.08	0.19/0.25
$Ca_8Mg_1Sr_1(PO_4)_6(OH)_2$			
a	1.34/1.33	0.17/0.17	0.16/0.17
b	1.29/1.33	0.34/0.17	0.15/0.17
c	1.30/1.33	0.12/0.17	0.15/0.17

materials with a high SSA; SSA values of the Mg-substituted materials are higher with respect to those of pure HA, and increase with the amount of Mg^{2+}. Measured mesopore volumes and areas were negligible for all materials and are not reported. All the studied materials showed a small amount of microporosity (see micropore area data reported in Table 3, third column). In the Mg^{2+}-only substituted HA there is a slight decrease in the micropore area values (not related to the Mg^{2+} content) in comparison with the pure HA.

Concerning the co-substitution, SSA values are higher with respect to the pure HA and there is a double effect: on one hand, the presence of Mg^{2+} causes an increase of SSA with respect to HA, and on the other hand, Sr^{2+} is responsible for a SSA decrease. The latter can be observed in both series with a constant Mg^{2+} content but varying Ca^{2+} and Sr^{2+} contents, and in the series with a fixed Ca^{2+} content and varying Mg^{2+} and Sr^{2+} contents. Comparing $Ca_9Mg_{0.1}Sr_{0.9}(PO_4)_6(OH)_2$ and $Ca_9Mg_{0.5}Sr_{0.5}(PO_4)_6(OH)_2$ samples with the same Ca^{2+} content, it is possible to single out that with an increase in Mg^{2+} content and a decrease in Sr^{2+} content the SSA becomes greater. Examining the $Ca_8Mg_{0.1}Sr_{1.9}(PO_4)_6(OH)_2$, $Ca_8Mg_{0.5}Sr_{1.5}(PO_4)_6(OH)_2$ and $Ca_8Mg_1Sr_1(PO_4)_6(OH)_2$ samples, at fixed Ca amount, with the increase of Mg^{2+} and the reduction of Sr^{2+} content there is also an increase of SSA. The microporosity decreases in all samples with respect to HA but without a specific trend; due to the low amount of micropores in all the materials the changes in the microporosity are not significant.

Generally, a decrease of the HA/β-TCP ratio (see XRPD data) shows some correlation with an increase in SSA.This is the first paper in which the influence on the SSA data of ions co-substituted in the HA structure is evaluated and reported.

Table 3 SSA and porosity data (N_2 adsorption at 77 K) of all synthesized samples. β-$Ca_3(PO_4)_2$ is reported as a reference

Samples	SSA (m^2/g)	t-plot micropore area (m^2/g)
$Ca_{10}(PO_4)_6(OH)_2$	73	3.4
β-$Ca_3(PO_4)_2$	125	/
$Ca_{9.9}Mg_{0.1}(PO_4)_6(OH)_2$	96	2.4
$Ca_{9.5}Mg_{0.5}(PO_4)_6(OH)_2$	107	2.3
$Ca_9Mg_1(PO_4)_6(OH)_2$	124	2.5
$Ca_9Mg_{0.1}Sr_{0.9}(PO_4)_6(OH)_2$	85	8.9
$Ca_9Mg_{0.5}Sr_{0.5}(PO_4)_6(OH)_2$	96	/
$Ca_8Mg_{0.1}Sr_{1.9}(PO_4)_6(OH)_2$	76	2.2
$Ca_8Mg_{0.5}Sr_{1.5}(PO_4)_6(OH)_2$	98	2.4
$Ca_8Mg_1Sr_1(PO_4)_6(OH)_2$	107	2.4

3.4 Raman spectroscopy

In Fig. 4, Section A, Raman spectra collected from Mg-substituted samples, with comparison to non-substituted samples, are reported. In all the spectra it is possible to single out the presence of an intense band at $\sim$910 cm^{-1} originating from symmetric stretching vibrations of O–P–O bonds. Additionally, bands at $\sim$390 (ν_2), 534 (ν_4), and 1,000 cm^{-1} (ν_3) correspond to characteristic vibrations of PO_4^{3-} groups in HA [37, 38]. The band at about 1,030 cm^{-1} can be assigned to CO_3^{2-} stretching vibration modes (ν_1) in a β-type carbonate apatite [39]. In Table 4 the main Raman band positions and assignments of hydroxyapatite are reported. In the case of the compositions modified with only Mg^{2+} ions it is possible to single out that the intensities of the full width at half maximum (FWHM) of the characteristic bands for HA at 910 cm^{-1} change. As the amount of Mg^{2+} increases (compare spectra of $Ca_{9.5}Mg_{0.5}(PO_4)_6(OH)_2$ and $Ca_9Mg_1(PO_4)_6(OH)_2$ with the reference spectra of α-TCP and β-TCP) more evidence is provided of the formation of a TCP phase with the appearance of a shoulder in the band located at $\sim$924 cm^{-1}.

Moreover, in order to better clarify the formation of a TCP phase, spectral deconvolutions in the spectral range between 940 and 880 cm^{-1} are reported in Fig. 4, Section B. Inspection of this figure shows that in the case of $Ca_{9.5}Mg_{0.5}(PO_4)_6(OH)_2$ and $Ca_9Mg_1(PO_4)_6(OH)_2$ the presence of two components (909 and 924 cm^{-1}) in the band centred at 910 cm^{-1} is clearly evident. This proves that the bands of the phosphate ions derive from a different apatite structure and are characteristic of a tricalcium phosphate structure, which also gives rise to a loss of crystallinity; the component at 924 cm^{-1} is typical of the β-TCP phase.

In Fig. 5, Section A the Raman spectra obtained from the co-substituted samples are shown. All spectra presented the main bands typical of an apatite structure described above. With the introduction of Sr^{2+} into the HA structure a shift of the main phosphate band toward low wavenumber (910 vs

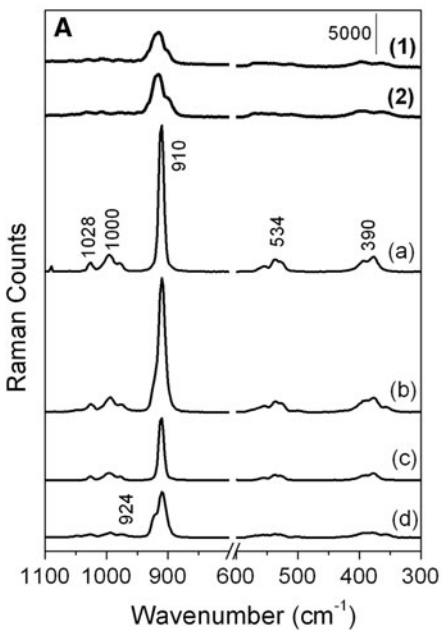

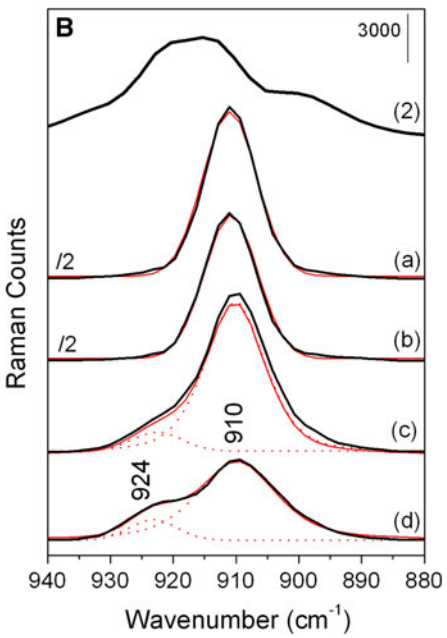

Fig. 4 *Section A*. Raman spectra of pure and Mg^{2+}-substituted HA samples in the spectral range of 1,100–300 cm^{-1}. Spectrum (*a*) $Ca_{10}(PO_4)_6(OH)_2$; spectrum (*b*) $Ca_{9.9}Mg_{0.1}(PO_4)_6(OH)_2$; spectrum (*c*) $Ca_{9.5}Mg_{0.5}(PO_4)_6(OH)_2$; spectrum (*d*) $Ca_9Mg_1(PO_4)_6(OH)_2$. Inserted reference materials: spectrum (*1*) α-$Ca_3(PO_4)_2$, spectrum (2) β-$Ca_3(PO_4)_2$. *Section B*. Spectral deconvolutions in the spectral range of 940–880 cm^{-1} carried out on the following samples: (*a*) $Ca_{10}(PO_4)_6(OH)_2$; (*b*) $Ca_{9.9}Mg_{0.1}(PO_4)_6(OH)_2$; (*c*) $Ca_{9.5}Mg_{0.5}(PO_4)_6(OH)_2$; (*d*) $Ca_9Mg_1(PO_4)_6(OH)_2$. Inserted reference material: spectrum (*2*) β-$Ca_3(PO_4)_2$

Table 4 Main Raman band positions and assignments of HA

Band positions (cm^{-1})	Band assignments
1,030	β type v_1 CO_3^{2-}
	Nondegenerate symmetric stretching
1,000	v_3 PO_4^{3-}
	P–O bonds antisymmetric stretching vibrations
910	v_1 PO_4^{3-}
	P–O bonds symmetric stretching vibrations
534	v_4 PO_4^{3-}
	O–P–O symmetric bending
390	v_2 PO_4^{3-}
	O–P–O symmetric bending

906 cm^{-1}) was clearly evident (see Fig. 5 Section B); this has previously been reported for the substitution of Sr^{2+} alone in HA by O'Donnell et al. [39]. This shift could be used to determine the change in Sr^{2+} in apatite compositions for in vitro and in vivo studies [39]. The $Ca_8Mg_{0.1}Sr_{1.9}(PO_4)_6(OH)_2$ composition, which is the sample with the highest Sr^{2+} content studied here, shows the greatest shift of the main phosphate band; moreover, comparing the samples with the same Ca^{2+} content (Spectrum (b) vs Spectrum (c) and Spectrum (d) *vs* Spectrum (e) vs Spectrum (f)), the increase of the amount of Mg^{2+} results in a broadening of the phosphate band. This feature is an index of a less crystalline sample and confirmed that the introduction of Mg^{2+} gives rise to the conversion to a TCP phase (see spectra in Fig. 4 carried out on the Mg^{2+}-substituted samples).

The stabilising effect on the HA phase of co-substitution of Sr^{2+} (for a Mg^{2+} substitution level of 0.5 mol) as observed by comparison of the HA/β-TCP content in Table 1, was also evident from the corresponding Raman spectra; comparing spectra of $Ca_{9.5}Mg_{0.5}(PO_4)_6(OH)_2$ and of $Ca_9Mg_{0.5}Sr_{0.5}(PO_4)_6(OH)_2$, (see Figs. 4b, 5b)shows, in the first case, a more pronounced shoulder at 924 cm^{-1} with respect to that of co-substituted sample, which showed only a small shoulder at 920 cm^{-1}.

The formation of a TCP phase in the co-substituted samples is less evident (Spectra (c) and (f), Fig. 5, Section B) than in the Mg^{2+}-substituted samples (Spectra (c) and (d), Fig. 4, Section B), but nevertheless a β-TCP phase is present in the co-substituted samples.

3.5 ATR spectroscopy

In Fig. 6 the ATR spectra for $Ca_{10}(PO_4)_6(OH)_2$ and Mg-substituted HA are reported. In the $Ca_{10}(PO_4)_6(OH)_2$ spectrum (Fig. 6 Section A), the intense bands originating from vibrations of PO_4^{3-} groups are seen. The most intense bands are 1090 and 1,045 cm^{-1}, assigned to triply degenerate antisymmetric vibrations (v_3) of P–O bonds. Other bands at 628, 602 and 563 cm^{-1} are due to triply degenerate bending vibrations (v_4) of O–P–O groups, typically well defined and sharp in the spectrum of a pure HA; the 963 cm^{-1} component is assigned to non-degenerate symmetric vibrations (v_1) of P–O bonds. The splitting of the v_4 vibrational band indicates the low site symmetry of the molecules, as three observed bands confirm the presence of more than one distinctive site for phosphate groups. Analysis of the spectra corresponding to the samples doped with Mg^{2+} showed a decrease in the intensity with the increase of Mg^{2+} content, of the 1,090, 953 and 628 cm^{-1} bands. The v_4 band changed from three peaks to two peaks in the sample with the highest Mg content; these spectral

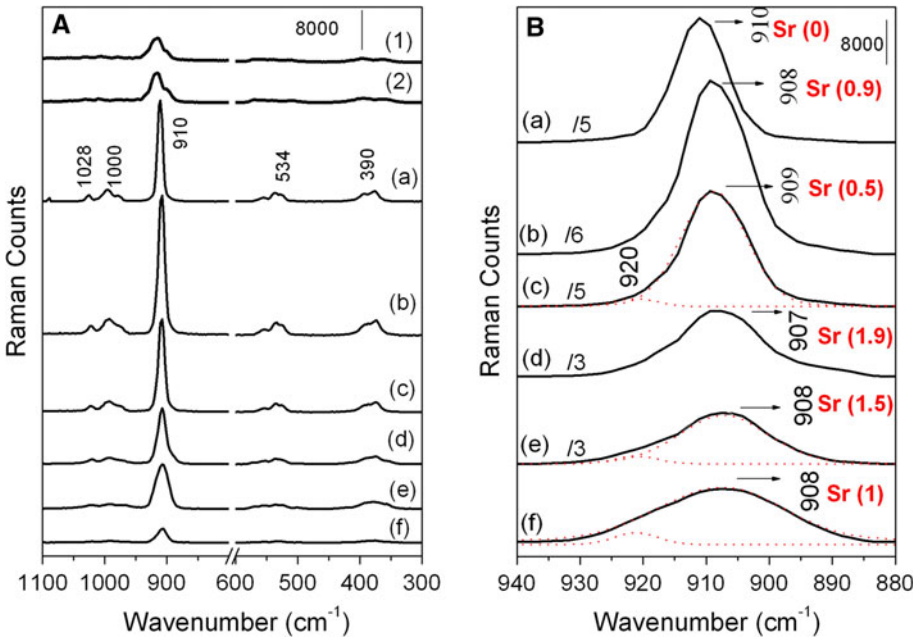

Fig. 5 *Section A.* Raman spectra of pure and Sr^{2+}- and Mg^{2+}-co-substituted HA samples in the spectral range of 1,100–300 cm^{-1}. Spectrum (*a*) $Ca_{10}(PO_4)_6(OH)_2$; spectrum (*b*) $Ca_9Mg_{0.1}Sr_{0.9}(PO_4)_6(OH)_2$; spectrum (*c*) $Ca_9Mg_{0.5}Sr_{0.5}(PO_4)_6(OH)_2$; spectrum (*d*) $Ca_8Mg_{0.1}Sr_{1.9}(PO_4)_6(OH)_2$; spectrum (*e*) $Ca_8Mg_{0.5}Sr_{1.5}(PO_4)_6(OH)_2$; spectrum (*f*) $Ca_8Mg_1Sr_1(PO_4)_6(OH)_2$. Inserted reference materials: spectrum (*1*) α-$Ca_3(PO_4)_2$, spectrum (*2*) β-$Ca_3(PO_4)_2$. *Section B.* Spectral deconvolutions in the spectral range of 940–880 cm^{-1} carried out on the pure and substituted HA samples

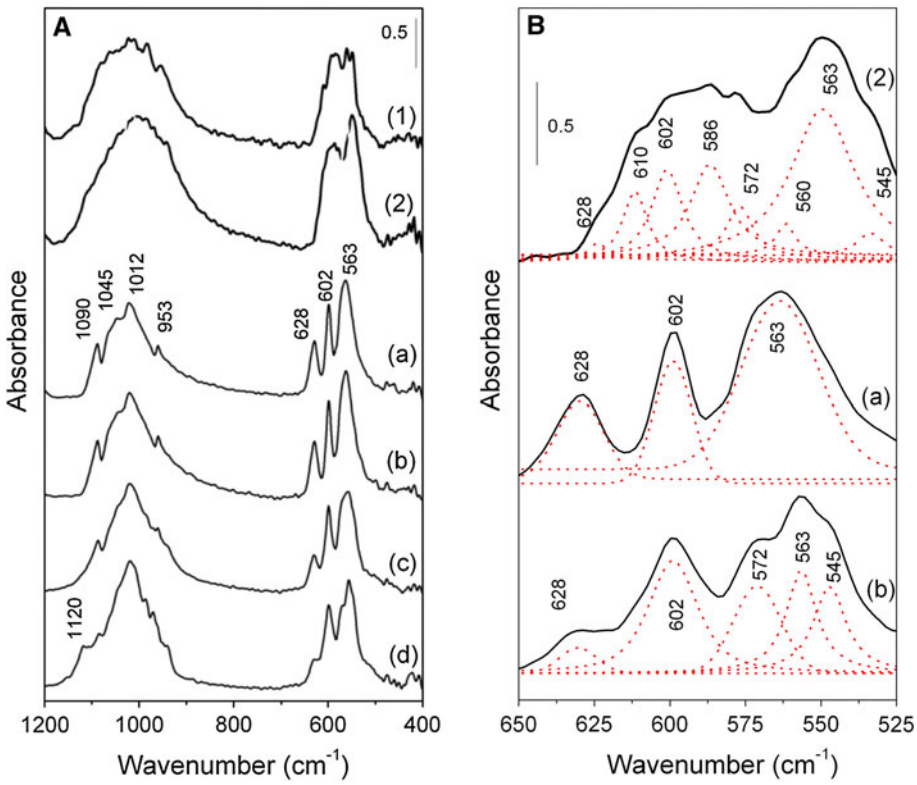

Fig. 6 *Section A.* ATR spectra of pure and Mg^{2+}-substituted HA samples in the spectral range of 1,200–400 cm^{-1}. Spectrum (*a*) $Ca_{10}(PO_4)_6(OH)_2$; spectrum (*b*) $Ca_{9.9}Mg_{0.1}(PO_4)_6(OH)_2$; spectrum (*c*) $Ca_{9.5}Mg_{0.5}(PO_4)_6(OH)_2$; spectrum (*d*) $Ca_9Mg_1(PO_4)_6(OH)_2$. Inserted reference materials: spectrum (1) α-$Ca_3(PO_4)_2$, spectrum (2) β-$Ca_3(PO_4)_2$. *Section B.* Spectral deconvolutions in the spectral range of 650–525 cm^{-1} carried out on the following samples: (*a*) $Ca_{10}(PO_4)_6(OH)_2$; (*b*) $Ca_9Mg_1(PO_4)_6(OH)_2$. Inserted reference material: spectrum (2) β-$Ca_3(PO_4)_2$

changes can be related to a decrease in the relative amount of HA phase as more β-TCP forms.

Moreover, in the case of the sample with the highest Mg^{2+} content, a band of low intensity at 1,120 cm^{-1} appears.

In Fig. 6, Section B the spectral deconvolutions in the spectral range of 650–525 cm^{-1} carried out on $Ca_{10}(PO_4)_6(OH)_2$ and $Ca_9Mg_1(PO_4)_6(OH)_2$ are reported; in the presence of Mg^{2+} two other components appear at 572 and 545 cm^{-1}, that are also evident in the deconvolutions carried out on the reference system β-TCP. So, in agreement with previous results, the presence of Mg^{2+} in the HA structure causes the formation of a β-TCP phase in addition to HA.

ATR spectra for $Ca_{10}(PO_4)_6(OH)_2$ and of co-substituted samples are shown in Fig. 7.

In all samples, it is possible to single out the main bands typical of HA structure. It is possible to notice that the presence of both Sr^{2+} and Mg^{2+} causes a decrease of sample crystallinity; the phosphate bands appear broad and not well resolved (see in detail the bands at 1,090 and 628 cm^{-1}). In Fig. 7 Section B the spectral deconvolutions in the spectral range of 650–525 cm^{-1} carried out on samples $Ca_{10}(PO_4)_6(OH)_2$, $Ca_9Mg_{0.5}Sr_{0.5}(PO_4)_6(OH)_2$ and $Ca_8Mg_1Sr_1(PO_4)_6(OH)_2$ are reported; in the presence of Mg^{2+} and Sr^{2+} the band located at 628 cm^{-1} disappears whereas two other components at 570 and 545 cm^{-1} are observed. These two components are also evident in the deconvolutions carried out on the reference system β-TCP.

These sentences are in agreement with results obtained from XRD analysis: the presence of Mg^{2+} and Sr^{2+} in the HA structure cause the formation of a TCP phase in addition to HA phase and a decrease of the sample crystallinity.

To summarize the ATR results, Table 5 reports the changes occurring in the phosphate bands in the Mg^{2+}-HA and Mg^{2+}–Sr^{2+}-HA substituted samples. The presence or absence (denoted by ✔ or ×, respectively) of the different phosphate groups typical of HA and TCP phases are reported.

With the introduction of only Mg^{2+}, the band at 953 cm^{-1} characteristic of the ν_1 phosphate vibrational mode becomes broader even at the lowest Mg^{2+} content; the pure β-TCP sample shows the same behaviour. Moreover, changes in the ν_4 phosphate vibrational modes are detectable at the highest Mg^{2+} content. Concerning the co-substituted HA, in all the samples it is evident that the ν_4 band changes from three peaks to two peaks. Moreover the OH stretching band located at ~3,570 cm^{-1} (spectral region not shown for the sake of brevity) decreases with increasing substitution.

Concerning the ν_3 PO_4^{3-} bands in the samples with the higher Mg^{2+} content (*i.e.* $Ca_8Mg_1Sr_1(PO_4)_6(OH)_2$, $Ca_8Mg_{0.5}Sr_{1.5}(PO_4)_6(OH)_2$, and $Ca_9Mg_1(PO_4)_6(OH)_2$) the 1,090 cm^{-1} component becomes broad according to the spectral features of TCP; this is further evidence of TCP formation in the presence of increasing amounts of Mg^{2+}.

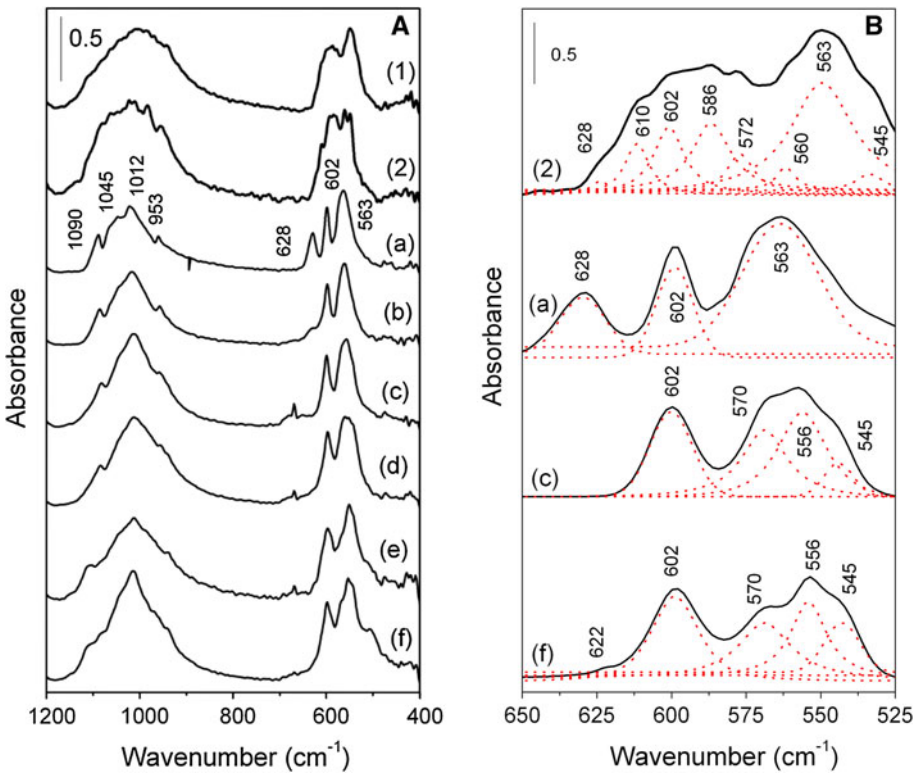

Fig. 7 ATR spectra of pure and Sr^{2+}- and Mg^{2+}- co-substituted HA materials in the spectral range of 1,200–400 cm^{-1}. Spectrum (*a*) $Ca_{10}(PO_4)_6(OH)_2$; spectrum (*b*) $Ca_9Mg_{0.1}Sr_{0.9}(PO_4)_6(OH)_2$; spectrum (*c*) $Ca_9Mg_{0.5}Sr_{0.5}(PO_4)_6(OH)_2$; spectrum (*d*) $Ca_8Mg_{0.1}Sr_{1.9}(PO_4)_6(OH)_2$; spectrum (*e*) $Ca_8Mg_{0.5}Sr_{1.5}(PO_4)_6(OH)_2$; spectrum (*f*) $Ca_8Mg_1Sr_1(PO_4)_6(OH)_2$. Inserted reference materials: spectrum (*1*) α-$Ca_3(PO_4)_2$, spectrum (*2*) β-$Ca_3(PO_4)_2$. *Section B.* Spectral deconvolutions in the spectral range of 650–525 cm^{-1} carried out on the following samples: (*a*) $Ca_{10}(PO_4)_6(OH)_2$; (*c*) $Ca_9Mg_{0.5}Sr_{0.5}(PO_4)_6(OH)_2$; (*f*) $Ca_8Mg_1Sr_1(PO_4)_6(OH)_2$. Inserted reference material: spectrum (*2*) β-$Ca_3(PO_4)_2$

Data derived from FT-IR spectra were found to be consistent with Raman data; clearly, some of the changes in the FTIR and Raman spectra correspond to the identified phases and their structural transformation observed by XRPD.

The combined use of XRPD, FTIR and Raman spectroscopies provides complementary data and indicates clearly phase formation and transformation as well as related structural changes resulting from the ions substituted in the HA structure. Our data suggests that the substitution of Sr^{2+} and Mg^{2+} ions into synthetic HA modifies some properties of HA (i.e. degree of crystallinity), and a co-substitution of 0.5 mol of both Mg and Sr ($Ca_9Mg_{0.5}Sr_{0.5}(PO_4)_6(OH)_2$) appears to stabilize the HA phase compared to a Mg-only substituted HA containing 0.5 mol Mg ($Ca_{9.5}Mg_{0.5}(PO_4)_6(OH)_2$).

Synthetic bone graft materials are an alternative to autologous bone, and currently hydroxyapatite-based ceramics represent the first choice in orthopaedic surgery, because they provide an osteoconductive scaffold to which mesenchymal stem cells can migrate and adhere, and can differentiate into functional osteoblasts [40]. Biphasic HA/β-TCP composite ceramics are widely used because of their biodegradable, biocompatible, and osteoconductive

Table 5 Presence or absence (denoted by ✔ or ×, respectively) of the different phosphate groups typical of HA and TCP phases for all the synthesized substituted HA samples as determined by ATR spectroscopy

Samples	PO_4^{3-} v_1 (953 cm^{-1})	PO_4^{3-} v_3 (1,090, 1,012 cm^{-1})	PO_4^{3-} v_4 (628, 602, 563 cm^{-1})
$Ca_{10}(PO_4)_6(OH)_2$	✔	✔✔	✔✔✔
$Ca_{9.9}Mg_{0.1}(PO_4)_6(OH)_2$	✔ (broad)	✔✔	✔✔✔
$Ca_{9.5}Mg_{0.5}(PO_4)_6(OH)_2$	✔ (broad)	✔✔	✔✔✔
$Ca_9Mg_1(PO_4)_6(OH)_2$	✔ (broad)	✔ (broad) ✔	✔ (broad) ✔
$Ca_9Mg_{0.1}Sr_{0.9}(PO_4)_6(OH)_2$	✔	✔✔	✔ (broad) ✔✔
$Ca_9Mg_{0.5}Sr_{0.5}(PO_4)_6(OH)_2$	✔	✔✔	×✔✔
$Ca_8Mg_{0.1}Sr_{1.9}(PO_4)_6(OH)_2$	✔	✔✔	×✔✔
$Ca_8Mg_{0.5}Sr_{1.5}(PO_4)_6(OH)_2$	✔ (broad)	✔ (broad) ✔	×✔✔
$Ca_8Mg_1Sr_1(PO_4)_6(OH)_2$	✔ (broad)	✔ (broad) ✔	×✔✔
α-$Ca_3(PO_4)_2$	✔ (broad)	×✔	×✔✔
β-$Ca_3(PO_4)_2$	✔ (broad)	×✔	×✔✔

characteristics [41, 42]. The mixtures of these two phases, also known as biphasic calcium phosphates (BCPs), are usually favoured for clinical applications because their resorption rate can be tuned to match the bone healing rate allowing to obtain a suitable balance between implant degradation and bone regeneration [43]. A recent study has also shown that BCP scaffolds can demonstrate osteoinductive properties [44].

In the present study, starting from a pure HA material and then systematically substituting either Mg^{2+} alone or Mg^{2+} and Sr^{2+} together in the structure we obtained BCP composite materials with a variable HA/β-TCP ratio.

In order to evaluate the behaviour towards osteoblast and osteoclast cells, biocompatibility and cytotoxicity studies will be carried out. The effects of both chemical composition and different HA/β-TCP phase ratios on cell behaviour requires evaluation, using Mg and Sr-free HA/β-TCP compositions with matching relative ratios of the two phases as controls. Based on these results, in vivo experiments will be performed in order to evaluate both the influence of the different phases (HA and/or β-TCP) and the effects of the element concentrations.

4 Conclusions

Magnesium ions are known to destabilise the HA structure, whereas strontium ions are known to substitute readily into the HA structure, retaining a single HA phase when heated to form a ceramic. In this study, a multi-technique approach was applied to HA derived samples and was used to investigate the effect of magnesium and strontium co-substitution in the HA structure and to identify clearly phase transformation and structural changes.

In all substituted samples, except that with the lowest amount of magnesium, formation of two phases with HA and β-TCP structure types was observed; the effects of the cations are correlated to the variation of cell parameters of both structures (expansion or contraction if the prevalent effect is due to strontium or magnesium, respectively). Other effects include the decrease of the crystallinity degree of HA and changing amounts of HA and β-TCP phases.

Starting from a pure HA material, with systematic substitutions we obtained BCP composite materials with variable HA/β-TCP ratios. By co-substitution at equimolar amounts (at a level of 0.5 mol) a BCP composition rich in the HA phase was obtained, whereas when only 0.5 mol of Mg was substituted (Sr free), the composition contained significantly more β-TCP phase.

Thus, prior choice of different molar ratios of the substituent cations allows us to design and obtain substituted materials with selected ratios of HA and β-TCP and also controlled degrees of crystallinity of HA.

Acknowledgments This work was financially supported by the Italian Ministry MUR (Project COFIN-2006, Prot. 2006032335_004: "Interface phenomena in silica-based nanostructured biocompatible materials contacted with biological systems"), by Regione Piemonte Italy (Project CIPE-2004: "Nanotechnologies and Nanosciences. Nanostructured materials biocompatible for biomedical applications") and by San Paolo company Project Id: ORTO11RRT5, whose contribution is gratefully acknowledged. V.A. kindly acknowledges Regione Piemonte, Italy, for a postdoctoral fellowship. FEI acknowledges ERASMUS programme for financial support during her research study at the University of Torino.

References

1. Qi G, Zhang S, Khor KA, Lye SW, Zeng X, Weng W, Liu C, Venkatraman SS, Ma LL. Osteoblastic cell response on magnesium-incorporated apatite coatings. Appl Surf Sci. 2008;255:304–7.
2. LeGeros RZ. Hydroxyapatite and related materials. Boca Raton: CRC Press; 1994.
3. LeGeros RZ. Calcium phosphates in oral biology and medicine. Basel: Karger; 1991.
4. Hong Y, Fan H, Li B, Guo B, Liu M, Zhang X. Fabrication, biological effects, and medical applications of calcium phosphate nanoceramics. Mater Sci Eng Reports. 2010;70:225–42.
5. Padilla S, Izquierdo-Barba I, Vallet-Regi M. High specific surface area in nanometric carbonated hydroxyapatite. Chem Mater. 2008;20:5942–4.
6. Sanchez-Salcedo S, Balas F, Izquierdo-Barba I, Vallet-Regi M. In vitro structural changes in porous HA/beta-TCP scaffolds in simulated body fluid. Acta Biomater. 2009;5:2738–51.
7. Zhou H, Lee J. Nanoscale hydroxyapatite particles for bone tissue engineering. Acta Biomater. 2011;7:2769–81.
8. Carrodeguas RG, De Aza S. alpha-Tricalcium phosphate: synthesis, properties and biomedical applications. Acta Biomater. 2011;7:3536–46.
9. de Lima IR, Alves GG, Soriano CA, Campaneli AP, Gasparoto TH, Ramos ES Jr, de Sena LA, Rossi AM, Granjeiro JM. Understanding the impact of divalent cation substitution on hydroxyapatite: an in vitro multiparametric study on biocompatibility. J Biomed Mater Res A. 2011;98A:351–8.
10. Ergun C, Webster TJ, Bizios R, Doremus RH. Hydroxylapatite with substituted magnesium, zinc, cadmium, and yttrium. I. Structure and microstructure. J Biomed Mater Res. 2002;59:305–11.
11. Lim PN, Tay BY, Chan CM, Thian ES. Synthesis and characterization of silver/silicon-cosubstituted nanohydroxyapatite. J Biomed Mater Res Part B Appl Biomater. 2012;100B:285–91.
12. Boanini E, Gazzano M, Bigi A. Ionic substitutions in calcium phosphates synthesized at low temperature. Acta Biomater. 2010;6:1882–94.
13. Manzano M, Lozano D, Arcos D, Portal-Nunez S, Lopez la Orden C, Esbrit P, Vallet-Regi M. Comparison of the osteoblastic activity conferred on Si-doped hydroxyapatite scaffolds by different osteostatin coatings. Acta Biomater. 2011;7:3555–62.
14. Bertinetti L, Drouet C, Combes C, Rey C, Tampieri A, Coluccia S, Martra G. Surface characteristics of nanocrystalline apatites: effect of Mg surface enrichment on morphology, surface hydration species, and cationic environments. Langmuir. 2009;25:5647–54.

15. Salviulo G, Bettinelli M, Russo U, Speghini A, Nodari L. Synthesis and structural characterization of Fe(3+)-doped calcium hydroxyapatites: role of precursors and synthesis method. J Mater Sci. 2011;46:910–22.
16. Drouet C, Carayon M-T, Combes C, Rey C. Surface enrichment of biomimetic apatites with biologically-active ions $Mg^{(2+)}$ and $Sr^{(2+)}$: a preamble to the activation of bone repair materials. Mat Sci Eng C Biomimetic Supramol Syst. 2008;28:1544–50.
17. Gibson IR, Bonfield W. Preparation and characterisation of magnesium/carbonate co-substituted hydroxyapatites. J Mater Sci Mater in Med. 2002;13:685–93.
18. Stephen JA, Skakle JMS, Gibson IR. Synthesis of novel high silicate-substituted hydroxyapatite by Co-substitution mechanisms. Key Eng Mater. 2007;87:330–2.
19. Kannan S, Goetz-Neunhoeffer F, Neubauer J, Pina S, Torres PMC, Ferreira JMF. Synthesis and structural characterization of strontium- and magnesium-co-substituted beta-tricalcium phosphate. Acta Biomater. 2010;6:571–6.
20. Laurencin D, Almora-Barrios N, de Leeuw NH, Gervais C, Bonhomme C, Mauri F, Chrzanowski W, Knowles JC, Newport RJ, Wong A, Gan Z, Smith ME. Magnesium incorporation into hydroxyapatite. Biomaterials. 2011;32:1826–37.
21. Nielsen SP. The biological role of strontium. Bone. 2004;35: 583–8.
22. Canalis E, Hott M, Deloffre P, Tsouderos Y, Marie PJ. The divalent strontium salt S12911 enhances bone cell replication and bone formation in vitro. Bone. 1996;18:517–23.
23. Buehler J, Chappuis P, Saffar JL, Tsouderos Y, Vignery A. Strontium ranelate inhibits bone resorption while maintaining bone formation in alveolar bone in monkeys (*Macaca fascicularis*). Bone. 2001;29:176–9.
24. Kolmas J, Jaklewicz A, Zima A, Bucko M, Paszkiewicz Z, Lis J, Slosarczyk A, Kolodziejski W. Incorporation of carbonate and magnesium ions into synthetic hydroxyapatite: the effect on physicochemical properties. J Mol Struct. 2011;987:40–50.
25. Suchanek WL, Byrappa K, Shuk P, Riman RE, Janas VF, TenHuisen KS. Preparation of magnesium-substituted hydroxyapatite powders by the mechanochemical-hydrothermal method. Biomaterials. 2004;25:4647–57.
26. Bertinetti L, Tampieri A, Landi E, Martra G, Coluccia S. Punctual investigation of surface sites of HA and magnesium-HA. J Eur Ceram Soc. 2006;26:987–91.
27. Landi E, Logroscino G, Proietti L, Tampieri A, Sandri M, Sprio S. Biomimetic Mg-substituted hydroxyapatite: from synthesis to in vivo behavior. J Mater Sci Mater Med. 2008;19:239–47.
28. PCPFWIN 2.3. JCPDS International center for diffraction data, Swarthmore 2002.
29. Landi E, Tampieri A, Celotti G, Sprio S. Densification behaviour and mechanisms of synthetic hydroxyapatites. J Eur Ceram Soc. 2000;20:2377–82.
30. Larson A, Von Dreele R. General structure analysis system (GSAS), Los Alamos National Laboratory Report LAUR 1994; 86-748.
31. Toby B. EXPGUI, a graphical user interface for GSAS. J Appl Crystallogr. 2001;34:210–9.
32. Sudarsanan K, Young RA. Acta Crystallogr. Sec B. 1969;25: 1534–9.
33. Dickens B, Schroeder L, Brown W. Crystallographic studies of the role of Mg as a stabilizing impurity in $Ca_3(PO_4)_2$. The crystal structure of pure $Ca_3(PO_4)_2$. J Solid State Chem. 1974;10:232–48.
34. Brunauer S, Emmett PH, Teller E. Adsorption of gases in multimolecular layers. J Am Chem Soc. 1938;60:309–19.
35. Ren F. Synthesis, characterization and ab initio simulation of magnesium-substituted hydroxyapatite. Acta Biomater. 2010;6: 2787–96.
36. Yasukawa A, Ouchi S, Kandori K, Ishikawa T. Preparation and characterization of magnesium-calcium hydroxyapatites. J Mater Chem. 1996;6:1401–5.
37. Aminzadeh A. Fluorescence bands in the FT-Raman spectra of some calcium minerals. Spectrochimica Acta Part a-Mol Biomol Spectrosc. 1997;53:693–7.
38. Silva CC, Sombra ASB. Raman spectroscopy measurements of hydroxyapatite obtained by mechanical alloying. J. Phys Chem Solids. 2004;65:1031–3.
39. O'Donnell MD, Fredholm Y, de Rouffignac A, Hill RG. Structural analysis of a series of strontium-substituted apatites. Acta Biomater. 2008;4:1455–64.
40. Paderni S, Terzi S, Amendola L. Major bone defect treatment with an osteoconductive bone substitute. La Chirurgia degli organi di movimento. 2009;93:89–96.
41. Lu X, Li S, Zhang J, Zhang Z, Lu B, Bu H, Li Y, Cheng J. Biocompatibility of HA/TCP biphasic ceramics with co-cultured human osteoblasts in vitro. J Biomed Eng. 2001;18:497–9.
42. Macchetta A, Turner IG, Bowen CR. Fabrication of HA/TCP scaffolds with a graded and porous structure using a camphene-based freeze-casting method. Acta Biomater. 2009;5:1319–27.
43. Arinzeh TL, Tran T, McAlary J, Daculsi G. A comparative study of biphasic calcium phosphate ceramics for human mesenchymal stem-cell-induced bone formation. Biomaterials. 2005;26: 3631–8.
44. Yuan H, Fernandes H, Habibovic P. Osteoinductive ceramics as a synthetic alternative to autologous bone grafting. Proc Natl Acad Sci USA. 2010;107:13614–9.